Biosensors and Bioelectronics 213 (2022) 114443

Contents lists available at ScienceDirect

Biosensors and Bioelectronics

journal homepage: www.elsevier.com/locate/bios

# Controlled synthesis of zinc-metal organic framework microflower with high efficiency electrochemiluminescence for miR-21 detection

Xiaoyan Wang [a], Xue Wang [a], Congyi Hu [a], Wan Guo [a], Xinjie Wu [a], Gaoxu Chen [a], Wenjie Dai [a], Shujun Zhen [a], Chengzhi Huang [b,**], Yuanfang Li [a,*]

[a] Key Laboratory of Luminescence Analysis and Molecular Sensing (Southwest University), Ministry of Education, College of Chemistry and Chemical Engineering, Southwest University, Chongqing, 400715, China

[b] Key Laboratory of Luminescent and Real-Time Analytical System (Southwest University), Chongqing Science and Technology Bureau, College of Pharmaceutical Sciences, Southwest University, Chongqing, 400715, China

ARTICLE INFO

*Keywords:*
Self-enhanced electrochemiluminesence
Dual ligand
Metal-organic framework
Resonance energy transfer
Biosensor

ABSTRACT

In this study, as the self-enhanced electrochemiluminescence (ECL) emitter, the dual ligand metal-organic framework microflower was successfully synthesized via a facile one-pot method by integrating 9,10-di(pcarboxyphenyl) anthracene (DPA) ligand and N, N-Diethylethylenediamine (DEAEA) ligand into zinc ions metal node, denoted as Zn-DPA/DEAEA (d-MOF). The DPA ligand was a typical ECL luminophore. The DEAEA ligand not only could be used as an effective co-reactant but also a morphologic regulator. The morphology of d-MOF changed from a thick sheet to a thin sheet and finally a microflower by controlling the dosage of DEAEA. Linking emitter and co-reactant in a MOF structure, the d-MOF exhibited an efficient intramolecular electron transfer process, with a strong and ultra-stable ECL performance without any extra co-reactants compared with the DPA ligand or the Zn-DPA single ligand MOF (s-MOF). Furthermore, an ECL resonance energy transfer (ECL-RET) biosensor was fabricated using d-MOF as donor, and 6-carboxy-4′, 5′-dichloro-2′, 7′-dimethoxyfluorescein (JOE) as accepter for the ultra-sensitive detection of miR-21 without additional co-reactant. And with a detection linear range of miR-21 was 100.0 aM to 10.0 pM, with a detection limit of 61.7 aM. This work offers a new perspective for the future design of stable self-enhanced ECL materials.

## 1. Introduction

Electrochemiluminescence (ECL) is redox-induced light emission, where luminophore is reduced or oxidized at the electrode to generate an excited state, and the electrochemical energy is converted into light energy (Wei et al., 2019b; Zhang et al., 2021a; Zhang et al., 2020b; Zou et al., 2020). On its advantages of operate simplicity, high sensitivity and low background signal, ECL has received increasing attention in the field of biosensing (Chen and Ding, 2022; Liao et al., 2019; Zanut et al., 2020; Zhou et al., 2020a; Zhou et al., 2020b). Given that the crucial role of efficient emitters in the construction and analytical ability of ECL biosensors, ranging from traditional luminescent materials, (inorganic metal complexes and organics) to emerging ECL luminophores (quantum dots, metal nanoparticles, clusters, perovskite nanocrystals, aggregation-induced emission materials), a series of emitters have been exploited for the construction of ECL biosensors (Cao et al., 2020; Guo et al., 2021; Li et al., 2017; Liu et al., 2015; Wang et al., 2020). Generally, to gain a high ECL signal, most ECL systems rely on intermolecular reactions between luminophores and co-reactants, requiring extraneous co-reactants to be added to the test solution (Cai et al., 2018; Luo et al., 2021; Tan et al., 2017; Zinna et al., 2019). Nevertheless, due to the long distance of electron transfer in intermolecular reaction, part of energy is lost, resulting in low electron transfer efficiency, measurement error and poor repeatability. Based on the previously consideration, more and more ECL systems have been developed without additional co-reactant. For example, Sun' steam first proposed to link Ru $(bpy)_3^{2+}$ emitter with the coreactant tripropylamine (TPA) via amide bonds to generate intramolecular ECL (Sun et al., 2009). Subsequently, some ECL materials that integrate luminophores and co-reactants into the same molecule have been reported successively (Duan et al., 2022; Gan et al., 2021; Ye et al., 2019). In addition, ECL systems based on polymer dots, NMOF-luminol, Fe–N–C SACs-luminol, etc. were

* Corresponding author.
** Corresponding author.
*E-mail addresses:* chengzhi@swu.edu.cn (C. Huang), liyf@swu.edu.cn (Y. Li).

https://doi.org/10.1016/j.bios.2022.114443
Received 23 February 2022; Received in revised form 23 May 2022; Accepted 30 May 2022
Available online 31 May 2022

developed using dissolved oxygen in the test solution as a co-reactant (Gu et al., 2020; Luo et al., 2019; Zhang et al., 2016). This ECL systems overcame the shortcomings of conventional ECL systems and gained high ECL emission even without exogenous co-reactants.

Metal-organic frameworks (MOFs) are porous crystalline materials composed of the coordination between metal ions or metal clusters and organic ligands (Jiang et al., 2020; Wang et al., 2022; Yang et al., 2022), with the advantages of large specific surface area, tunable structure, abundant active sites, and can be used as an excellent sensing platform (Wang et al., 2021c; Zhang et al., 2020a). MOFs can be precisely adjusted to display their specific performance through carefully designing metal nodes and organic ligands (Yu et al., 2020). Particularly, compared with single-ligand MOF, dual-ligand MOF combine ligands with different functions to achieve bifunctionalization, and are widely used in various fields. For instance, Yin and his co-workers prepared a dual ligand MOF with dipicolinic acid and 2-aminoterephthalic acid as ligands and $Eu^{3+}$ ions as metal node, exhibiting dual fluorescence emission characteristics for the ratiometric detection of HClO (Sun et al., 2021). Zhang's group presented a dual ligand MOF based on 9, 10-anthracenyl bis (benzoic acid) ligand and tetrakis (4-carboxyphenyl) porphyrin ligand to achieve reversible binding to $O_2$ (Zeng et al., 2019). Lei's group proposed a mixed-ligand MOF by coassembly of 9,10-di (p-carboxyphenyl)-anthracene (DPA) and 1,4-diazabicyclo [2.2.2] octane to the same framework, for self-enhanced ECL without additional coreactants (Zhu et al., 2021). Based on the shorter electron transfer pathway within the molecule, dual-ligand MOFs offer a promising alternative in the field of ECL.

Herein, using DPA as the organic light-emitting ligand, N, N-Diethylethylenediamine (DEAEA) ligand as the co-reactant, and zinc ions as the metal node, the Zn-DPA/DEAEA dual ligand metal-organic framework microflower (d-MOF) was exploited by a facile one-pot method (Scheme 1A). The obtained $DEAEA^{\cdot}$ reacted with $DPA^{+}$ via intramolecular electron transfer (ICT) to generate excited d-MOF, resulting in self-enhanced ECL emission. Moreover, microRNA-21 (miR-21) is considered an important cancer marker and is necessary to achieve its ultrasensitive detection (Zhang et al., 2021b). To verify the detection capability of d-MOF, combined with the amplification strategy of catalytic hairpin assembly (CHA), utilizing d-MOF as the donor and 6-carboxy-4′, 5′-dichloro-2′, 7′-dimethoxyfluorescein (JOE) as the receptor, an ECL resonance energy transfer (ECL-RET) biosensor was constructed for ultrasensitive detection of miR-21 without additional co-reactant (Scheme 1B). Firstly, deposition of d-MOF on glassy carbon electrode (GCE) as the analytical platform for strong anodic ECL emission. The H1 was connected to the electrode via the Au–S bond. Then, in the presence of the miR-21 target, a large amount of JOE was introduced on the electrode by the CHA amplification, so as to be close to the d-MOF, the ECL intensity of d-MOF was declined due to the effect of the ECL-RET. Thus, the self-enhanced ECL biosensor designed in this paper realized the detection of miR-21 with high sensitivity.

## 2. Experimental

### 2.1. Materials and apparatus

The materials and apparatus were supplied in the supplementary material. The nucleic acid sequences were shown in Table S1.

### 2.2. Preparation of MOFs

The Zn-DPA single ligand MOF (s-MOF) was prepared according to the reported literature before (Zhu et al., 2021). The d-MOF was prepared via a hydrothermal method. In brief, a mixture of 14.3 mg Zn $(NO_3)_2{\cdot}6H_2O$ (48.0 μmol), 20 mg DPA (48.0 μmol) and 35 μL DEAEA was suspended in 3 mL N,N-Dimethylformamide (DMF), and dispersed by ultrasound for 30 min. The mixture was then heated in a Teflon-lined autoclave at 120 °C for 24 h. Next, the obtained d-MOF was collected after centrifugation at 8000 rpm for 5 min, then washed twice with DMF and ultrapure water, respectively. Finally, the d-MOF was lyophilized, and then the d-MOF was dispersed in ultrapure water for subsequent experiments.

### 2.3. Mott-Schottky plot measurement

Firstly, 5 μL d-MOF dispersion (1.0 mg/mL) was dripped onto the polished electrode and dried at room temperature under air conditions. Then, the Mott-Schottky plot of d-MOF was investigated in 0.1 M deoxygenated $Na_2SO_4$ solution at different frequencies (1000 Hz, 1500 Hz and 2000 Hz).

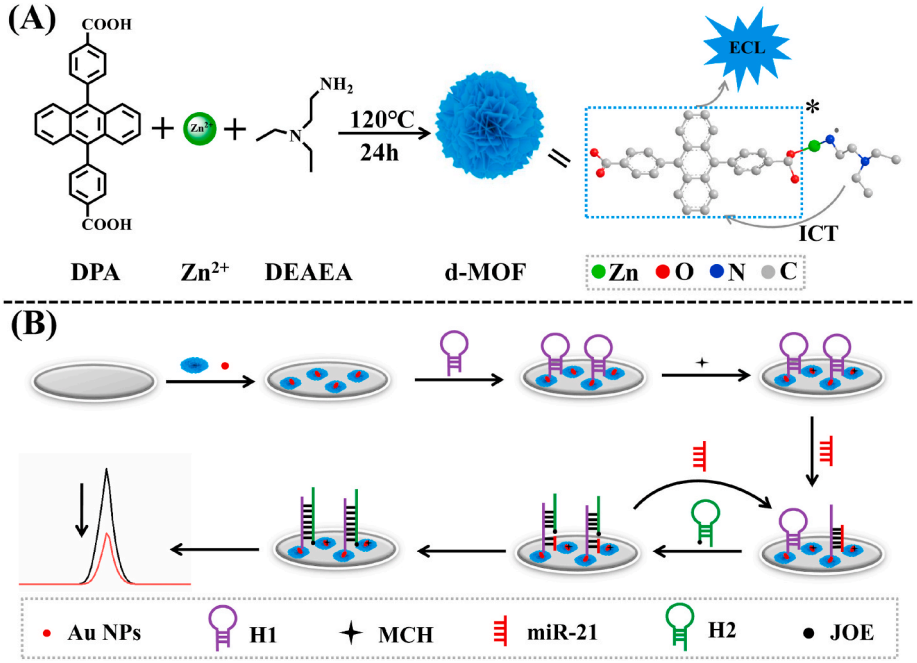


**Scheme 1.** (A) The synthesis and possible self-enhanced ECL mechanism of d-MOF.(B) Fabrication process of this ECL-RET biosensor.

### 2.4. Electrophoresis characterization

Agarose gel electrophoresis was executed to monitor the stepwise assembly processes of CHA. The hairpin H1 and H2 were annealed at 95 °C for 5 min, respectively, and then slowly cooled for 2 h at 25 °C. These samples were then incubated at 37 °C (approximately 70 min) and mixed with loading buffer. Then, the agarose gel electrophoresis was proceeded at the TBE buffer (0.5 × ), the voltage was 120 V, and the electrophoresis time was about 50 min. Last, the electrophoresis photo was analyzed by the imaging system.

### 2.5. Preparation of ECL measurement

Firstly, the GCEs were ground carefully with 0.3 μm and 0.05 μm $Al_2O_3$ powder, followed by rinsing in ethanol and water, respectively, to obtain a cleaned GCE. Subsequently, 5 μL of d-MOF (1.0 mg/mL) was added dropwise to the GCE surface by coating adsorption and dried. ECL experiments were performed in 0.1 M pH 7.4 phosphate buffer saline (PBS). The potential sweep range was −2 V–0.7 V, and the scan rate was set as 0.3 V/s, with a photomultiplier tube (PMT) of 800 V.

### 2.6. Fabrication of ECL biosensor

Firstly, 5 μL d-MOFs (1.0 mg/mL) and 5 μL gold nanoparticles (Au NPs, 8.0 nM, 50 nm) dispersion were casted onto the electrode surface, respectively, and then dried. The scanning electron microscopy (SEM) image of Au NPs loaded d-MOF was characterized (Fig. S1), indicating that Au NPs were uniformly dispersed on the d-MOF surface. Following, the H1 (5 μL, 1.0 μM) was poured onto the surface of electrodes and then reacted overnight at 4 °C. The non-specific binding site was blocked by 5 μL 6-Mercapto-1-hexanol (MCH, 1.0 mM) solution. Afterwards, 5 μL of different concentrations of miR-21 solution were spread on the surface of electrodes and then incubated at 37 °C (about 75 min). Then, the H2 (5 μL, 1.0 μM) was propagated onto the electrodes and mixed (37 °C, 75 min). The electrodes were carefully rinsed three times with PBS buffer after each modification step. Last, the prepared biosensor was tested in 0.1 M PBS (pH 7.4) buffer.

### 2.7. Human sample detection

The obtained blood samples were clotted for 2 h at room temperature, and then the clotted samples were collected by centrifugation for 10 min at 3000 rpm. The standard sample of miR-21 was added to serum samples for detection.

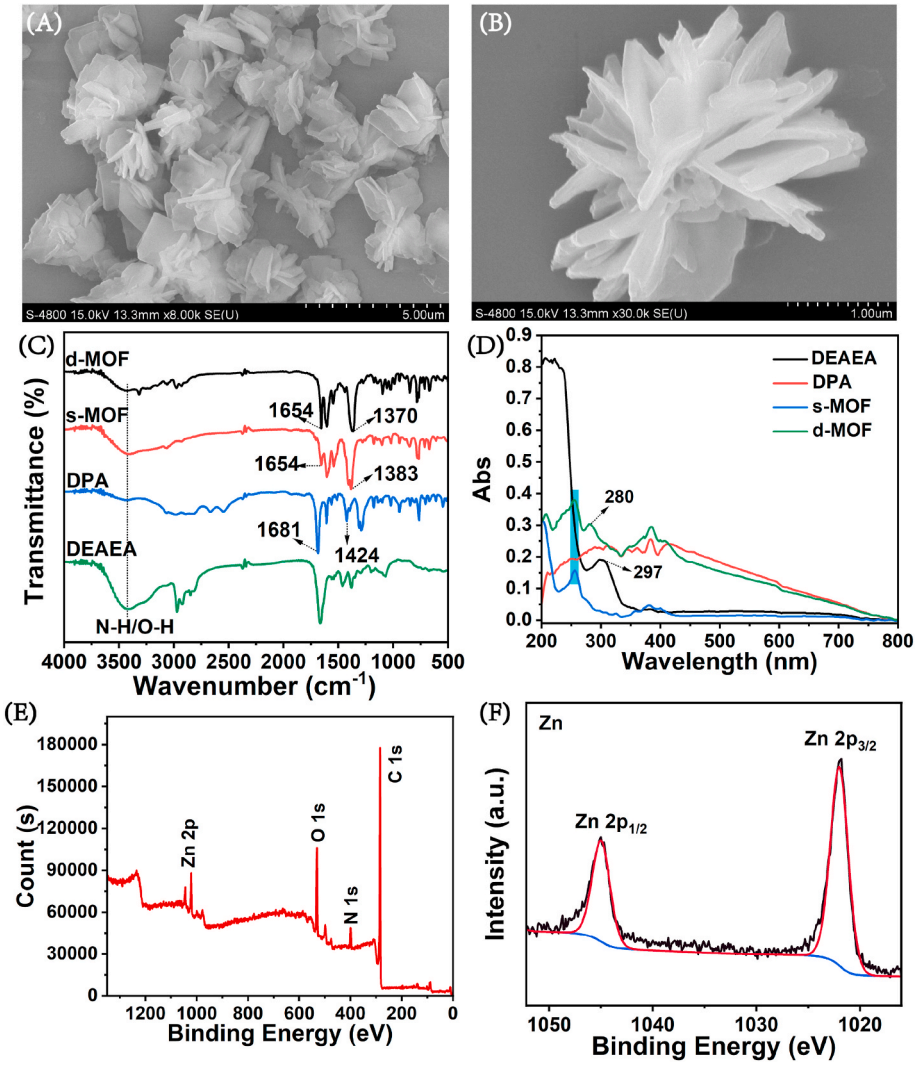


**Fig. 1.** SEM images of d-MOF (A–B). (C) FT-IR spectra and (D) UV–vis absorption spectra of DEAEA, DPA, s-MOF, and d-MOF. (E) Survey XPS spectrum and (F) Zn 2p XPS spectra of d-MOF.

## 3. Results and discussion

### 3.1. Characterization of the d-MOF

The morphology of the as-prepared MOFs was described by SEM, the dual ligand MOFs with different morphology were gained via controlling the dosage of DEAEA (Fig. S2). Accordingly, as the volume of DEAEA increased, the dual ligand MOFs were formed into thick flakes first, then flakes, and finally microflowers. The microflower-like d-MOF was obtained through the self-aggregation of sheets (Fig. 1A and B). Interestingly, the ECL behaviors of the dual ligand MOFs with different morphologies were similar (Fig. S3). Thus, microflower-shaped d-MOF was selected as ECL emitter in subsequent studies. The Fourier transform infrared (FT-IR) spectrum of DPA (Fig. 1C) exhibited the representative peaks at 1681 and 1424 $cm^{-1}$ corresponding to C═O stretching in –COOH and C═O stretching of the benzene ring, respectively (Zhao et al., 2022). The shoulder peaks in s-MOF were moved to 1654 and 1383 $cm^{-1}$, respectively, and the sharp peaks of d-MOF were moved to 1654 and 1370 $cm^{-1}$, respectively, confirmed the coordination of the carbonyl group of DPA with $Zn^{2+}$. Since the stretching vibrations of N–H and O–H in the above materials were both around 3435 $cm^{-1}$ (Xiong et al., 2022). To demonstrate the existence of the DEAEA ligand in d-MOF, the structural features of DEAEA, DPA, s-MOF and d-MOF were described by UV–vis spectra (Fig. 1D). The multiple absorption peaks of DPA at 320–400 nm were also observed in s-MOF and d-MOF. Compared with DPA, both s-MOF and d-MOF showed a new absorption peak at 256 nm, indicating successful coordination with zinc ions. In addition, there was only one obvious absorption peak in DEAEA at 297 nm. The absorption peak of DEAEA was shifted to 280 nm after d-MOF was formed.

The surface elements composition and chemical valence of d-MOF were analyzed by X-ray photoelectron spectroscopy (XPS) spectrum. As exhibited in Fig. 1E, the XPS displayed obvious peaks of C 1s, N 1s, O 1s, and Zn 2p, showing that these elements were abundant in d-MOF. In particular, for the high-resolution XPS of Zn 2p (Fig. 1F), the peaks at 1044.9 and 1021.8 eV originated from Zn $2p_{1/2}$ and Zn $2p_{3/2}$, indicating that the bivalent Zn was the major in the d-MOF (Fang et al., 2020; Yan et al., 2019). The powder X-ray diffraction (PXRD) pattern of the d-MOF was analyzed, the major PXRD diffraction peaks at $2\theta$ = 6.3°, 12.0°, 12.7°, 13.9°, 16.1°, 16.8°, 18.9°, 22.5° and 23.6° were clearly seen (Fig. S4). Herein, these sharp diffraction peaks indicated that d-MOF with a crystal structure.

### 3.2. ECL performance of d-MOF

To study the self-enhanced ECL of d-MOF, the ECL signals of modified electrodes such as GCE, DPA, s-MOF, and d-MOF were first studied under different conditions. As seen in Fig. 2A, the anode ECL signals of DPA, s-MOF and d-MOF were observed in PBS (pH 7.4) without any co-reactants. It is well known that bare GCE had no obvious ECL signal in PBS buffer (Fig. S5). There was also almost no ECL signal of GCE in PBS containing 10.0 mM DEAEA (Fig. 2A, insert). The ECL intensity of DPA was 1300 a.u. in the first cycle, with continuous scanning, the signal was also unstable and the intensity decays rapidly (Fig. 2B). Even if the ECL signal of s-MOF was strong at around 17,800 a.u, the signal declined sharply until it became extremely weak (Fig. 2C). This showed that alone DPA or s-MOF was not a good ECL luminophore in the anode ECL system in the absence of adding co-reactants. After adding 10 mM DEAEA in PBS, a strong ECL signal with stability up to about 300 s could be obtained in s-MOF (Fig. S6), illustrating DEAEA could be used as an effective anode co-reactant as previously reported (Wang et al., 2016). Particularly, the d-MOF had a strong ECL signal (approximately 17,799 a.u.). The d-MOF could still maintain good stability even in continuous scanning for 900 s, and with a relative standard deviation (RSD) of 0.21% without co-reactant (Fig. 2D). This might be due to the integration of the two ligands into d-MOF, DPA as an emitter, DEAEA as the self-coreactant, and the effective intramolecular electron transfer between the two ligands, with less energy loss, and the electron transfer path was shorter. The electron transfer efficiencies of DPA, s-MOF, and d-MOF were investigated by electrochemical impedance spectroscopy (EIS, Fig. S7). Compared with the DPA or s-MOF modified electrodes, the impedance of d-MOF modified electrodes was lower, which might be due to its unique framework micro-flower structure that accelerated

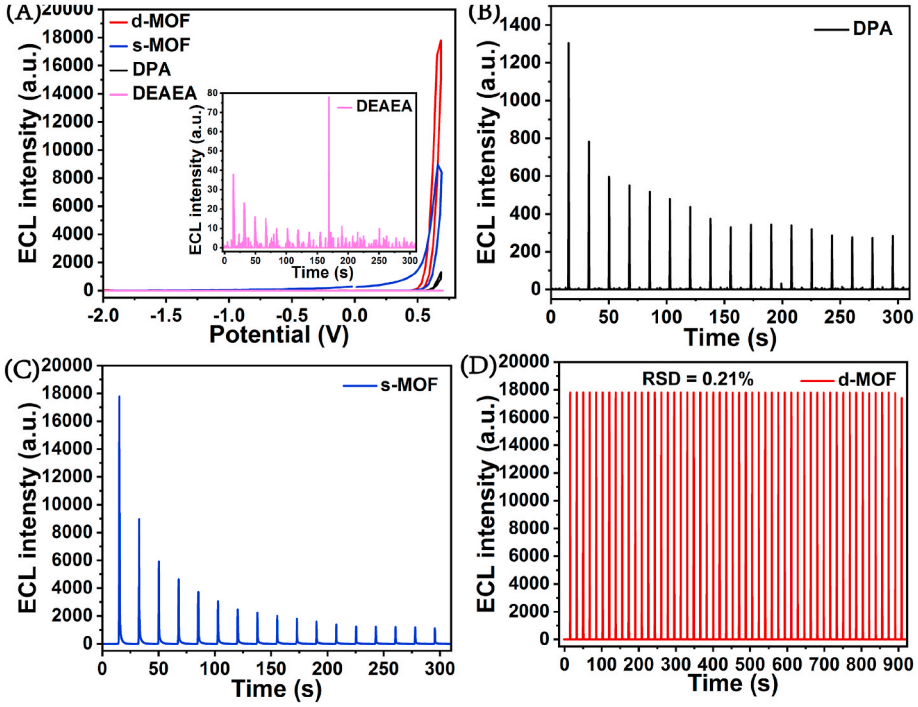


**Fig. 2.** (A) ECL curves of electrodes modified with different materials in 0.1 M, pH 7.4 PBS. Inset: ECL-time curve of GCE with 10.0 mM DEAEA in PBS (0.1 M, pH 7.4). ECL-time curves of electrodes decorated with different luminescent materials: (B) DPA, (C) s-MOF, and (D) d-MOF in 0.1 M PBS (pH 7.4). The concentrations of all materials were 1.0 mg/mL.

electron transfer (Zhu et al., 2021). Moreover, the stability of the ECL signal of d-MOF was studied continuously for 30 days (Fig. S8), the intensity was almost unchanged. In brief, compared with DPA or s-MOF, d-MOF showed superior ECL signal, and longer stability, and was an ideal self-enhanced ECL luminophore.

### 3.3. ECL mechanism

The effect of dissolved oxygen on this self-enhanced ECL of d-MOF was first investigated (Fig. S9). There was almost no difference in the ECL intensity of d-MOF whether in the $N_2$-saturated, air or in $O_2$-saturated PBS. That was, no other co-reactants in this ECL system. Moreover, compared with the fluorescence (FL) emission peak (452 nm), the ECL emission (523 nm) of d-MOF emerged a red shift of about 71 nm (Fig. 3A).

To investigate the reason for the red-shift of the ECL emission wavelength of d-MOF, the band structure of d-MOF was analyzed. Firstly, The UV–vis diffuse reflectance spectrum of d-MOF was measured (Fig. S10A). Based on the Tauc plot method (Jin et al., 2021), the energy gap (Eg) of d-MOF was estimated to be approximately 2.92 eV (Fig. 3B), which confirmed that d-MOF was a semiconductor (Cui et al., 2021). To obtain the specific location of the conduction band (CB) of the d-MOF, the Mott–Schottky (MS) plot was performed (Fig. 3C). The positive slope of this MS plot exhibited the d-MOF was an n-type semiconductor (Cui et al., 2020; Wei et al., 2019a). The flat band potential ($E_{fb}$) of d-MOF was estimated to be −0.35 V (*vs.* RHE) from the abscissa of the MS curve intersection. Since the minimum value of the conduction band of an n-type semiconductor was generally negative about 0.2 eV than its $E_{fb}$ (Li et al., 2021), the conduction band energy ($E_{CB}$) of d-MOF was estimated to be −0.55 eV. The valence band energy ($E_{VB}$) of d-MOF was calculated as 2.37 eV from a band gap equation ($E_{VB} = Eg + E_{CB}$) (Wang et al., 2021a), and the calculated $E_{VB}$ was similar to the measured valence band XPS spectrum (Fig. S10B). According to the above results, the energy band structure of d-MOF was obtained and as shown in Fig. 3D. Hence, d-MOF was an n-type semiconductor, the excited state of d-MOF* could be generated by a lower energy surface state instead of a band gap transition, otherwise the ECL spectrum should be the same as the FL spectrum (Chen et al., 2017; Wu et al., 2014).

In view of the above discussion, a possible self-enhanced ECL mechanism for d-MOF was proposed. According to the classic ECL mechanism (Wang et al., 2021b), the DEAEA ligand in d-MOF was first oxidized at the anode to form $DEAEA^{+}$ radicals. Next, $DEAEA^{+}$ radicals were deprotonated to generate $DEAEA^{\cdot}$. Meanwhile, the DPA ligand in d-MOF was electrochemically oxidized to generate $DPA^{+}$ radicals. Following that, the obtained $DEAEA^{\cdot}$ radicals reacted with the $DPA^{+}$ radicals through ICT to produce an excited state of d-MOF, and ECL was generated when the excited state of d-MOF returned to the ground state. Equations 1-5 described the possible ECL mechanism of d-MOF:

$$\text{d-MOF(DEAEA)} - e^{-} \rightarrow \text{d-MOF(DEAEA)}^{+} \quad (1)$$

$$\text{d-MOF(DEAEA)}^{+} \rightarrow \text{d-MOF(DEAEA)}^{\cdot} + H^{+} \quad (2)$$

$$\text{d-MOF(DPA)} - e^{-} \rightarrow \text{d-MOF(DPA)}^{+} \quad (3)$$

$$\text{d-MOF(DPA)}^{+} + \text{d-MOF(DEAEA)}^{\cdot} \rightarrow \text{d-MOF*} + \text{products} \quad (4)$$

$$\text{d-MOF*} \rightarrow \text{d-MOF} + h\nu \quad (5)$$

### 3.4. Detection principle of the proposed ECL-RET biosensor

On the basis of the above advantages, the d-MOF had excellent ECL performance and was suitable to be used as a substrate material of the ECL biosensor. Considering the excellent ECL signal and suited ECL wavelength of d-MOF. The ECL-RET biosensor was constructed using d-MOF as donor and JOE as receptor for the ultrasensitive detection of miR-21. The UV–vis spectrum of H2-JOE was studied (Fig. 4A). The absorption peak between 220 nm and 300 nm was derived from H2, and the absorption peak at 400–600 nm was derived from JOE. Obviously, the absorption spectrum of JOE had a good overlap with the ECL spectrum of d-MOF, which proved that the ECL-RET strategy was feasible (Fig. 4A, inset).

To validate the feasibility of this signal amplification system, the CHA cycle was monitored by agarose gel electrophoresis (Fig. 4B). The

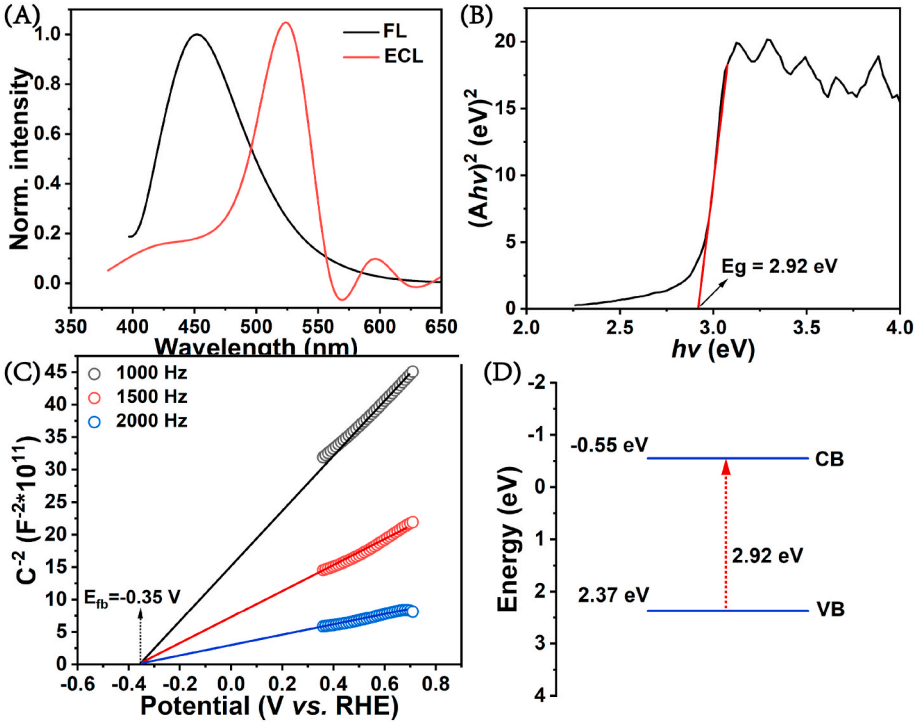


**Fig. 3.** (A) FL and ECL spectrum, (B) the Tauc plot, (C) the Mott-Schottky plots, and (D) the band structure of d-MOF.

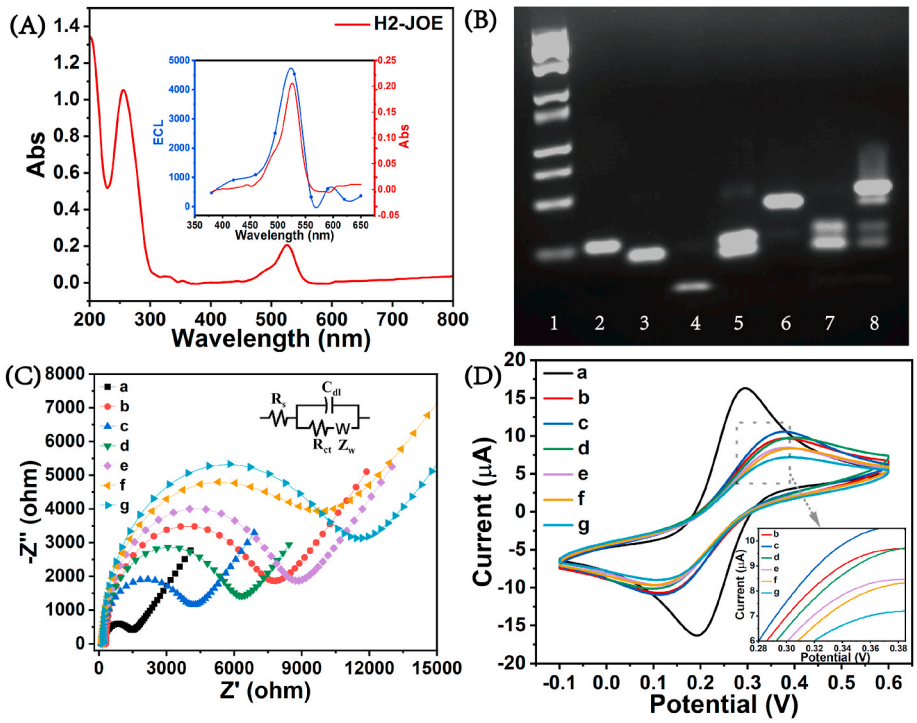


**Fig. 4.** (A) UV–vis absorption of H2-JOE. Inset: the overlap between the UV–vis absorption spectrum of JOE and the ECL spectrum of d-MOF. (B) agarose gel electrophoresis image of CHA. Lane 1, Maker; lane 2, H1; lane 3, H2; lane 4, miR-21; lane 5, H1+H2; lane 6, miR-21+H1; lane 7, miR-21+H2; lane 8, miR-21+H1+H2. (C) EIS and (D) CV characterization of (a) GCE, (b) d-MOF/GCE, (c) Au NPs/d-MOF/GCE, (d) H1/Au NPs/d-MOF/GCE, (e) MCH/H1/Au NPs/d-MOF/GCE, (f) miR-21/MCH/H1/Au NPs/d-MOF/GCE, and (g) H2/miR-21/MCH/H1/Au NPs/d-MOF/GCE in 5.0 mM $[Fe(CN)_6]^{3-/4-}$ solution with 0.1 M KCl. Inset: magnified CV curves image.

channels from 1 to 8 were associated with Marker, H1, H2, miR-21, H1+H2, miR-21+H1, miR-21+H2, and miR-21+H1+H2, respectively. The H1 was difficult to hybridize with H2 without miR-21, even after annealing. When incubated with miR-21, H1 and H2, miR-21 rapidly hybridized with H1 and catalyzed H1 and H2 hybridization. The clear bands of miR-21 further suggested that miR-21 could be replaced and released by H2, and repeated multiple reaction cycles, indicating that this CHA was effectively triggered.

To verify the successful construction of this biosensor, the cyclic voltammetry (CV) and EIS characterizations were measured. As shown in Fig. 4C, an extremely small electron transfer resistance (Ret) was acquired from the GCE (curve a). On account of the poor conductivity of d-MOF, the Ret increased after d-MOF was dripped on the electrode (curve b). Owing to the good electrical conductivity of Au NPs, the Ret was declined when Au NPs were modified on the d-MOF/GCE surface (curve c). After layer-by-layer modification of H1 (curve d), MCH (curve e), miR-21 (curve f), and H2 (curve g), the Ret increased gradually. Hence, the EIS results clearly elucidated that the successfully fabrication of this biosensor. As pictured in Fig. 4D, GCE showed a pair of clear redox peaks (curve a). After assembling d-MOF, the redox peak current descended since the hindrance of d-MOF on the electron transfer process (curve b). After the Au NPs assembled on the d-MOF/GCE surface, the current increased significantly owing to the good conductivity of Au NPs (curve c). Then, fixed of H1 (curve d), MCH (curve e), miR-21 (curve f), and H2 (curve g), the current of the biosensor continuously decreased on account of the electron transfer process of the non-electrochemically active materials was hindered, indicating that the successful preparation of the ECL biosensor. Furthermore, the ECL characterizations were also studied (Fig. S11), there was almost no ECL response on GCE (curve a). Similar ECL intensities were discovered in curves b to f, which were attributed to the ECL emission of d-MOF. The ECL signal of this biosensor descended significantly only after CHA incubation (curve g). Thus, all the above results indicated that the preparation of the biosensor was successful.

### 3.5. Detection performance of the proposed ECL-RET biosensor

To achieve a good analytical ability, some interrelated factors such as the concentrations of d-MOF and Au NPs, the pH value of PBS, the incubation time of miR-21 and H2 had been optimized. The results displayed that the best concentration of Au NPs was 8.0 nM (Fig. S12). The most suitable detection condition of the PBS was pH 7.4 (Fig. S13). The optimal concentration of d-MOF was 1.0 mg/mL (Fig. S14). The optimal incubation time of miR-21 was 75 min (Fig. S15). The best incubation time of H2 was 75 min (Fig. S16).

Under the best experimental conditions, the detection ability of the ECL biosensor was studied. As exhibited in Fig. 5A, the ECL intensities declined gradually correspondingly with increasing miR-21 concentration. A satisfying linear relationship between the ECL signals and the logarithmic concentration of miR-21 in a detection scope of 100.0 aM to 10.0 pM was observed (Fig. 5B). The linear fitting equation was depicted as $I = 15565.6–2509.2 \lg c_{miR\text{-}21}$, (where $I$ represented the ECL intensity, $R^2 = 0.996$). The limit of detection (LOD) was calculated to be 61.7 aM with reference to the equation of $I_L = I_B + k\ s_B$ (Wang et al., 2021c), where the $I_B$ represented the average ECL intensity of the control group, the $k$ was a numerical factor chosen according to the confidence level desired and a value of 3, and the $s_B$ represented the standard deviation of the control group measurements (n = 7, $s_B$ = 65.8). The analysis performance of other methods to detect miR-21 was compared Table S2 and showing that this biosensor offered a potential platform for detecting miR-21.

Furthermore, the selectivity of this ECL-RET biosensor for miR-21, including in a blank and miR-107, miR-141 and miR-155, was investigated (Fig. S17). ECL intensity decreased significantly only in the presence of target miR-21. Seven sensing platforms were constructed and 100.0 fM miR-21 was selected to evaluate the reproducibility of the ECL strategy, showing a relatively impressive reproducibility (Fig. S18).

In addition, to verify the practicality, the spiked recovery of miR-21 in human serum was investigated using standard addition method. As displayed in Table S3, this ECL strategy exhibited a good recovery rate ranged from 93.3% to 107.2%, and with a relatively low RSD, declaring a good practicality for real samples detection of miR-21.

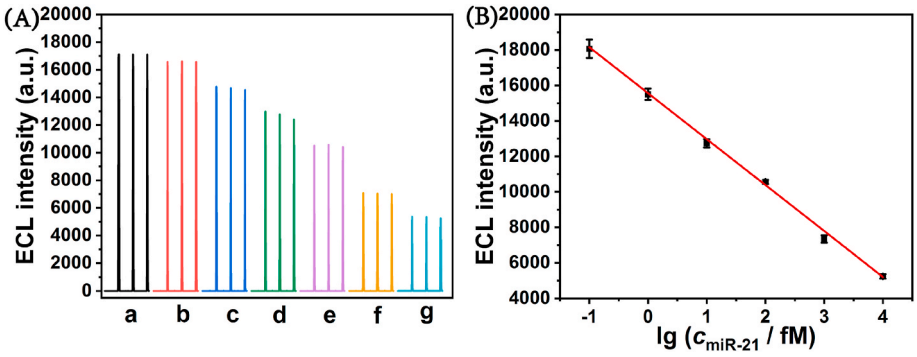


**Fig. 5.** (A) The ECL response of this proposed biosensor with different miR-21 concentrations: (a) 0, (b) 100.0 aM, (c) 1.0 fM, (d) 10.0 fM, (e) 100.0 fM, (f) 1.0 pM, and (g) 10.0 pM. (B) The calibration plot between ECL intensity and the logarithm concentrations of miR-21.

## 4. Conclusion

In summary, we successfully prepared the d-MOF through a simple one-pot strategy by integrating DPA ligand and DEAEA ligand into a zinc ion node for self-enhanced ECL. The d-MOF exhibited a stronger and more stable ECL signal than DPA alone or s-MOF due to the shortened intramolecular electron transfer distance. Particularly, the DEAEA ligand acted as an efficient co-reactant and morphology regulator, and by controlling the amount of DEAEA, the morphology of d-MOF was transformed from thick flake to thin flake and finally to microflower. Moreover, an ECL-RET biosensor was proposed by using d-MOF as donor and JOE as accepter for ultra-sensitive miR-21 detection without additional co-reactant. This work not only opens the way for designing high-quality dual-ligand MOF, but also broadens the application of self-enhanced MOF materials in the ECL biosensing field. We confirmed that d-MOF has excellent ECL signals and analytical performance, but the d-MOF only with anodic ECL signals and the biosensor is disposable. The development of dual-ligand MOF with both cathodic and anodic ECL signals and the construction of reusable biosensor are still worth studying in future research.

## CRediT authorship contribution statement

**Xiaoyan Wang:** Investigation, Conceptualization, Methodology, Data curation, Analysis, Validation, Writing – original draft, Formal analysis. **Xue Wang:** Conceptualization, Methodology, Formal analysis. **Congyi Hu:** Conceptualization, Methodology. **Wan Guo:** Methodology, Formal analysis. **Xinjie Wu:** Methodology, Formal analysis. **Gaoxu Chen:** Methodology, Investigation. **Wenjie Dai:** Methodology, Conceptualization. **Shujun Zhen:** Supervision, Methodology. **Chengzhi Huang:** Supervision, Formal analysis, Writing – review & editing. **Yuanfang Li:** Data curation, Funding acquisition, Formal analysis, Writing – review & editing.

## Declaration of competing interest

The authors declare that they have no known competing financial interests or personal relationships that could have appeared to influence the work reported in this paper.

## Acknowledgments

This work was financially supported by the National Natural Science Foundation of China (NSFC, no. 21874109).

## Appendix A. Supplementary data

Supplementary data to this article can be found online at https://doi.org/10.1016/j.bios.2022.114443.

## References

Cai, X.L., Zheng, B., Zhou, Y., Younis, M.R., Wang, F.B., Zhang, W.M., Zhou, Y.G., Xia, X. H., 2018. Chem. Sci. 9, 6080–6084.
Cao, Y., Zhu, W.L., Wei, H.F., Ma, C., Lin, Y.H., Zhu, J.J., 2020. Anal. Chem. 92, 4123–4130.
Chen, Y., Zhou, S., Li, L., Zhu, J.-j., 2017. Nano Today 12, 98–115.
Chen, Y.H., Ding, Z.F., 2022. Curr. Opin. Electrochem. 32, 100901.
Cui, W.R., Li, F.F., Xu, R.H., Zhang, C.R., Chen, X.R., Yan, R.H., Liang, R.P., Qiu, J.D., 2020. Angew. Chem. Int. Ed. 59 (40), 17684–17690.
Cui, W.R., Zhang, C.R., Xu, R.H., Chen, X.R., Yan, R.H., Jiang, W., Liang, R.P., Qiu, J.D., 2021. ACS EST Water 1, 440–448.
Duan, Y., Song, Y., Fan, N.K., Yao, Y.Z., Deng, S.X., Ding, S.J., Shen, B., Yin, Q.F., 2022. Biosens. Bioelectron. 197, 113784.
Fang, Y., Wang, H.M., Gu, Y.X., Yu, L., Wang, A.J., Yuan, P.X., Feng, J.J., 2020. Anal. Chem. 92 (4), 3206–3212.
Gan, X.F., Han, D.B., Wang, J.M., Liu, P., Li, X.R., Zheng, Q.Y., Yan, Y.R., 2021. Biosens. Bioelectron. 171, 112735.
Gu, W.L., Wang, H.J., Jiao, L., Wu, Y., Chen, Y.X., Hu, L.Y., Gong, J.M., Du, D., Zhu, C.Z., 2020. Angew. Chem. Int. Ed. 59, 3534–3538.
Guo, Y.M., Yang, F.Z., Yao, Y., Li, J.S., Cheng, S.T., Dong, H.W., Zhang, H., Xiang, Y.D., Sun, X., 2021. J. Hazard Mater. 401, 123794.
Jiang, Z.W., Zou, Y.C., Zhao, T.T., Zhen, S.J., Li, Y.F., Huang, C.Z., 2020. Angew. Chem. Int. Ed. 59, 3300–3306.
Jin, J.K., Wu, K., Liu, X.Y., Huang, G.Q., Huang, Y.L., Luo, D., Xie, M., Zhao, Y., Lu, W., Zhou, X.P., He, J., Li, D., 2021. J. Am. Chem. Soc. 143, 21340–21349.
Li, L.L., Chen, Y., Zhu, J.J., 2017. Anal. Chem. 89, 358–371.
Li, Y.J., Cui, W.R., Jiang, Q.Q., Wu, Q., Liang, R.P., Luo, Q.X., Qiu, J.D., 2021. Nat. Commun. 12 (1), 4735.
Liao, X.J., Fu, H.M., Yan, T.T., Lei, J.P., 2019. Biosens. Bioelectron. 146, 111743.
Liu, Z.Y., Qi, W.J., Xu, G.B., 2015. Chem. Soc. Rev. 44, 3117–3142.
Luo, J.H., Li, Q., Chen, S.H., Yuan, R., 2019. ACS Appl. Mater. Interfaces 11, 27363–27370.
Luo, R., Lv, H., Liao, Q., Wang, N., Yang, J., Li, Y., Xi, K., Wu, X., Ju, H., Lei, J., 2021. Nat. Commun. 12 (1), 6808.
Sun, S.G., Yang, Y., Liu, F.Y., Fan, J.L., Peng, X.J., Kehr, J., Sun, L.C., 2009. Dalton Trans. 7969–7974.
Sun, Y.Q., Cheng, Y., Yin, X.B., 2021. Anal. Chem. 93, 3559–3566.
Tan, X., Zhang, B., Zou, G.Z., 2017. J. Am. Chem. Soc. 139, 8772–8776.
Wang, Q.C., Ma, J., Li, G., Zhao, T.X., Chen, P., Liu, F., Yin, S.F., 2021a. J. Mater. Chem. 9, 27041–27048.
Wang, T.Y., Wang, D.C., Padelford, J.W., Jiang, J., Wang, G.L., 2016. J. Am. Chem. Soc. 138, 6380–6383.
Wang, X., Jiang, Z., Yang, C., Zhen, S., Huang, C., Li, Y., 2022. J. Hazard Mater. 423, 126978.
Wang, X.Y., Xiao, S.Y., Yang, C.P., Hu, C.Y., Wang, X., Zhen, S.J., Huang, C.Z., Li, Y.F., 2021b. Anal. Chem. 93, 14178–14186.
Wang, Y.G., Zhao, G.H., Chi, H., Yang, S.H., Niu, Q.F., Wu, D., Cao, W., Li, T.D., Ma, H. M., Wei, Q., 2021c. J. Am. Chem. Soc. 143, 504–512.
Wang, Z., Pan, J., Li, Q., Zhou, Y., Yang, S., Xu, J.J., Hua, D., 2020. Adv. Funct. Mater. 30 (30), 2000220.
Wei, S., Zhang, F., Zhang, W., Qiang, P., Yu, K., Fu, X., Wu, D., Bi, S., Zhang, F., 2019a. J. Am. Chem. Soc. 141 (36), 14272–14279.
Wei, X., Zhu, M.J., Cheng, Z., Lee, M., Yan, H., Lu, C., Xu, J.J., 2019b. Angew. Chem. Int. Ed. 58 (10), 3162–3166.
Wu, P., Hou, X.D., Xu, J.J., Chen, H.Y., 2014. Chem. Rev. 114, 11027–11059.
Xiong, H.W., Huang, Z.P., Lin, Q.Y., Yang, B., Yan, F., Liu, B.H., Chen, H., Kong, J.L., 2022. Anal. Chem. 94, 837–846.
Yan, M.X., Ye, J., Zhu, Q.J., Zhu, L.P., Huang, J.S., Yang, X.R., 2019. Anal. Chem. 91, 10156–10163.
Yang, C., Jiang, Z., Wu, Q., Hu, C., Huang, C., Li, Y., Zhen, S., 2022. J. Colloid Interface Sci. 605, 214–222.
Ye, J., Liu, G.Y., Yan, M.X., Zhu, Q.J., Zhu, L.P., Huang, J.S., Yang, X.R., 2019. Anal. Chem. 91, 13237–13243.

Yu, K.H., Wei, T.X., Li, Z.J., Li, J.Y., Wang, Z.Y., Dai, Z.H., 2020. J. Am. Chem. Soc. 142, 21267–21271.
Zanut, A., Fiorani, A., Canola, S., Saito, T., Ziebart, N., Rapino, S., Rebeccani, S., Barbon, A., Irie, T., Josel, H.P., Negri, F., Marcaccio, M., Windfuhr, M., Imai, K., Valenti, G., Paolucci, F., 2020. Nat. Commun. 11 (1), 2668.
Zeng, J.Y., Wang, X.S., Qi, Y.D., Yu, Y., Zeng, X., Zhang, X.Z., 2019. Angew. Chem. Int. Ed. 58, 5692–5696.
Zhang, B., Kong, Y., Liu, H., Chen, B., Zhao, B., Luo, Y., Chen, L., Zhang, Y., Han, D., Zhao, Z., Tang, B.Z., Niu, L., 2021a. Chem. Sci. 12, 13283–13291.
Zhang, G., Chai, H., Tian, M., Zhu, S., Qu, L., Zhang, X., 2020a. Anal. Chem. 92 (10), 7354–7362.
Zhang, G.Y., Cai, C., Cosnier, S., Zeng, H.B., Zhang, X.J., Shan, D., 2016. Nanoscale 8, 11649–11657.
Zhang, N., Gao, H., Jia, Y.L., Pan, J.B., Luo, X.L., Chen, H.Y., Xu, J.J., 2021b. Anal. Chem. 93, 6857–6864.
Zhang, Y.P., Zhao, Y.Q., Han, Z.G., Zhang, R.Z., Du, P.Y., Wu, Y.X., Lu, X.Q., 2020b. Angew. Chem. Int. Ed. 59, 23261–23267.
Zhao, L., Wang, M., Song, X., Liu, X., Ju, H., Ai, H., Wei, Q., Wu, D., 2022. Chem. Eng. J. 434, 134691.
Zhou, J.J., Li, Y., Wang, W.J., Tan, X.C., Lu, Z.C., Han, H.Y., 2020a. Biosens. Bioelectron. 164, 112332.
Zhou, Y.L., Yin, H.S., Zhao, W.W., Ai, S.Y., 2020b. Coord. Chem. Rev. 424, 213519.
Zhu, D., Zhang, Y., Bao, S.S., Wang, N.N., Yu, S.Q., Luo, R.G., Ma, J., Ju, H.X., Lei, J.P., 2021. J. Am. Chem. Soc. 143, 3049–3053.
Zinna, F., Voci, S., Arrico, L., Brun, E., Homberg, A., Bouffier, L., Funaioli, T., Lacour, J., Sojic, N., Di Bari, L., 2019. Angew. Chem. Int. Ed. 58, 6952–6956.
Zou, R., Teng, X., Lin, Y.J., Lu, C., 2020. Trends Anal. Chem. 132, 116054.